Polarized Nuclei in Normal and Superconducting Rhodium

T. A. Knuuttila, J. T. Tuoriniemi, K. Lefmann [b],
K. I. Juntunen, F. B. Rasmussen, [c] and K. K. Nummila [1]

Low Temperature Laboratory, Helsinki University of Technology, P.O. Box 2200, FIN-02015 HUT, Finland

[b] *Dept. Cond. Matt. Phys. and Chem., Risø National Laboratory, 4000 Roskilde, Denmark*

[c] *Niels Bohr Institute, University of Copenhagen, Universitetsparken 5, 2100 København Ø, Denmark*

REPORT TKK-KYL-002

July 2000

ISBN 951-22-5105-1

ISSN 1455-0806

---

[1] Present address: VTT Automation, Measurement Technology, P.O. Box 1304, FIN-02044 VTT, Finland

Abstract

We have performed SQUID-NMR measurements on rhodium nuclei at ultra-low temperatures. With initial polarizations of up to $p = 0.95$, the susceptibility data showed clear indications of an antiferromagnetic tendency, but nevertheless no signs of nuclear magnetic ordering. The lowest actually measured nuclear temperature was 280 pK, whereas the lowest nuclear temperatures achieved were below 100 pK. Double and triple-spin-flip resonance lines were detected, yielding direct information of the interactions between the nuclear spins. The superconducting transition was observed with the critical values, $T_c = 210$ μK and $B_c(0) = 3.4$ μT. Measurements with polarized nuclei were performed also in the superconducting state, where the effect of superconductivity on the spin-lattice relaxation rate was studied. The spin-lattice relaxation time was longer in the superconducting state at all temperatures.

1 Introduction

1.1 Background

Studies of nuclear magnetic ordering in metals have become experimentally feasible by the development of advanced cooling techniques, and thereby the spontaneously ordered phase of the nuclear spins has been observed in a few metals at the nano- and microkelvin regime [1]. The starting point for the theoretical understanding of nuclear magnets is usually better than that of electronic systems, since the interactions between the nuclear spins are often fairly simple and can be well understood from first principles. In metals the important processes are the dipolar interaction and the indirect conduction electron mediated exchange interaction. In pure metals spontaneous nuclear magnetic ordering has so far been observed in Cu in 1982 [2] and Ag in 1991 [3].

Rhodium is an interesting candidate for studies of nuclear magnetic ordering, as it not only has suitable properties for practical experiments, but it is also a superconductor. This provides the possibility to study the effect of the coherent conduction electron system on the polarized nuclear spins and vice versa. Experiments aiming for the ordered state in Rh were started in the early 1990's [4].

Rhodium is a very unique superconductor, as the critical parameters of the transition are extremely low, $T_c = 0.3$ mK and $B_c = 5$ μT [5]. In order to adiabatically switch a sample with polarized nuclei between the normal and superconducting (sc) states, the critical field of the transition must be lower than the internal local field $B_{\rm loc}$ of the nuclear spins, as the leading non-constant term of the entropy of the spin system is proportional to $(B^2 + B_{\rm loc}^2)$ and B is changed abruptly to zero at the sc transition. In rhodium this condition is fulfilled, since the critical field B_c is much lower than the local field, $B_{\rm loc} = 34$ μT [5,6].

1.2 The spin Hamiltonian

Rhodium, consisting of a single natural isotope with $I = \frac{1}{2}$, has no isotopic effects or quadrupolar interactions. The spin Hamiltonian of rhodium can be split into four terms: dipolar, Rudermann-Kittel (RK) exchange, anisotropic indirect exchange, and Zeeman interactions,

$$\mathcal{H} = \mathcal{H}_{\rm dip} + \mathcal{H}_{\rm RK} + \mathcal{H}_{\rm ae} + \mathcal{H}_{\rm Z}. \tag{1.1}$$

The anisotropic exchange term $\mathcal{H}_{\rm ae}$ results from indirect exchange interaction mediated by the d-electrons [6,7]. As a practical approximation, the dipolar and anisotropic exchange terms can be combined to

$$\mathcal{H}_{\rm dip} + \mathcal{H}_{\rm ae} = \tfrac{1}{2}\sum_{i,j} \frac{\mu_0 \hbar^2 \gamma_{\rm eff}^2}{4\pi r_{ij}^3}[\mathbf{I}_i \cdot \mathbf{I}_j - 3(\mathbf{I}_i \cdot \hat{\mathbf{r}}_{ij})(\mathbf{I}_j \cdot \hat{\mathbf{r}}_{ij})], \tag{1.2}$$

where

$$\gamma_{\rm eff}^2 = \gamma^2 + \frac{4\pi r_{ij}^3 \tilde{B}_{ij}}{\mu_0 \hbar^2}, \tag{1.3}$$

is the effective gyromagnetic ratio including the coefficients $\tilde{B}_{ij}$ representing the pseudodipolar exchange [8]. The RK-coupling is of the form

$$\mathcal{H}_{\rm RK} = -\tfrac{1}{2}\sum_{i,j} J_{ij} \mathbf{I}_i \cdot \mathbf{I}_j, \tag{1.4}$$

where J_{ij} is the coupling constant between spins at sites i and j. The values of J_{ij} and $\tilde{B}_{ij}$ can in principle be found from band structure calculations, but no such study has been performed for rhodium. Finally the Zeeman term is

$$\mathcal{H}_{\rm Z} = -\hbar\gamma \mathbf{B} \cdot \sum_i \mathbf{I}_i, \tag{1.5}$$

where $\mathbf{B}$ is the external magnetic field and $\gamma/2\pi = 1.34$ MHz/T is the gyromagnetic ratio of rhodium, with $\mu = -0.088\mu_N$.

The relative magnitude of the RK and the dipolar interactions are conventionally described by the parameter

$$R = \sum_j J_{ij}/(\mu_0 \hbar^2 \gamma^2 \rho), \tag{1.6}$$

where ρ is the number density of spins. However, due to the anisotropic exchange the gyromagnetic ratio appears larger than its bare value so that it is feasible to define,

$$R_{\rm eff} = \sum_j J_{ij}/(\mu_0 \hbar^2 \gamma_{\rm eff}^2 \rho). \tag{1.7}$$

For rhodium the experiments indicate $(\gamma_{\rm eff}/\gamma)^2 = 1.4 \pm 0.1$ and $R_{\rm eff} = -0.9 \pm 0.1$, whereas taking the pure dipolar interaction gives $R = -1.2 \pm 0.1$ [9].

1.3 Effective field

In mean field theory the effective field has the form [10]

$$\mathbf{B}_{\rm eff} = \mathbf{B} + (R + L - D)(\frac{\gamma_{\rm eff}}{\gamma})^2 \mu_0 p \mathbf{M}_{\rm sat}, \tag{1.8}$$

where L is the Lorentz factor from long range dipolar interactions and has the value $1/3$ for a cubic lattice, D is the demagnetization factor, p the nuclear polarization and $\mu_0 \mathbf{M}_{\rm sat} = \mu_0 \gamma \hbar \rho/2 = 40.5$ μT the saturation magnetization. The fluctuating local field $B_{\rm loc}$ does not contribute in mean field theory. Such a description by an effective field is, however, not fully accurate because the anisotropic exchange has a limited range (due to the electron mean free path), so that the dipolar D is not necessarily applicable to the anisotropic exchange contribution.

Within this formalism, the static susceptibility is given by

$$\chi'(0) = \chi_0/[1 - (R + L - D)(\frac{\gamma_{\rm eff}}{\gamma})^2 \chi_0], \tag{1.9}$$

where $\chi_0 = \lambda/T$ is the Curie susceptibility with $\lambda = \mu_0 \hbar^2 \gamma^2 N_A/4V_m k_B = 1.3$ nK for rhodium. Substituting χ_0 into Eq. (1.9) gives the Curie-Weiss law

$$\chi'(0) = \frac{\lambda}{T - \theta}, \tag{1.10}$$

with the Weiss temperature $\theta = \lambda(R + L - D)(\frac{\gamma_{\rm eff}}{\gamma})^2$.

2 Experimental setup and methods

The experiments were performed in the new cascade nuclear demagnetization cryostat at the Low Temperature Laboratory in Helsinki [11]. The first nuclear stage of the cryostat is a massive sliced copper cylinder, with 98 moles effectively in the 9 T field, precooled by a powerful dilution refrigerator. The sample acts as a second nuclear cooling stage and can be polarized with a 7.5 T magnet.

2.1 Rhodium sample

The rhodium sample was a slab-shaped single crystal with dimensions $0.4 \times 5 \times 25$ mm^3 from a commercial manufacturer [12]. The nominal purity of the rhodium was 99.99%. The major impurities as specified by the supplier are listed in Table 1.

Table 1
Impurity concentrations in the Rh sample according to the manufacturer's analysis.

Impurity	Ag	Al	Au	C	Cl	Co	Cr	Cu
ppm	< 0.1	2.0	0.9	15	3.0	0.2	2.5	0.4
Impurity	Fe	H	Mg	Mn	Mo	N	Na	Ni
ppm	15	< 1.0	0.03	1.0	2.0	< 5.0	0.2	< 1.0
Impurity	Pt	O	Si	Ti	Ta	V	W	Zr
ppm	10	6.0	10	1.0	0.3	0.2	10	2.0

The stated crystal orientation of the sample was such that the short edge of 0.4 mm, defined as the geometrical x-axis, is aligned with [110] (see Fig. 1). The longest axis, z, is close to [001], misaligned by 7°.

The demagnetization field for such a sample can be approximated to good accuracy by that of an ellipsoid with corresponding primary axes. The measures

yield the demagnetization factors 0.91, 0.08 and 0.01, along the dimensions 0.4, 5 and 25 mm respectively [13].

For an ultra-low temperature experiment, good thermal conductivity of the sample is essential. Thus a heat treatment for improving the transport properties is a crucial step in the sample preparation. A heat treatment of the noble and platinum-group metals in a low oxygen pressure not only anneals the crystal structure, but also neutralizes impurities by selective oxidization and precipitation [14–16].

The heat treatment conditions for rhodium were optimized by experimenting with several foil samples. The best results were obtained at a high temperature, above 1400°C, and a low pressure of about 1 μbar of pure oxygen [17]. A temperature closer to the melting point of Rh at 1966°C would probably have been beneficial, but the maximum operating temperature of our vacuum oven was 1550°C.

The single crystal sample was annealed in several steps, first at 1300°C and later at 1530°C, in 0.4 μbar pure O_2. After a total of 16 days of treatment the resulting RRR value was 740. About 15% of the mass of the sample was evaporated during the treatment.

The sample was fixed to the top of the copper nuclear stage through a thermal link made of copper and silver. The silver link and the sample were connected by diffusion welding. Before this a 400 nm silver layer was evaporated onto the connecting surfaces of the Rh sample. The diffusion welding was done at 500°C at a low oxygen pressure for 5 h. The contact resistance at 4.2 K was measured to be 40 nΩ. The silver link with the sample was then joined to the copper link by electron beam welding and the whole assembly was annealed at a low oxygen pressure at 500°C for 2 h. Finally the assembly was mounted on top of the copper nuclear stage. The low temperature electrical resistance of the link to the middle of the sample was estimated to be about 500 nΩ, where more than half of the resistance is due to the sample itself. The Wiedemann-Franz relation thus gives a thermal resistance of ≈ 20 K^2/W.

For shielding the sample from the remnant field of the large polarizing magnet, a cylindrical shield manufactured from a high permeability material, Cryoperm-10 [18], was placed around the sample setup inside the bore of the magnet. The length of the shield was 110 mm with an inner diameter of 23 mm and wall thickness 1.5 mm. The low temperature shielding factor was better than 1000 and the shield saturated in an external field of about 10 mT.

In a cascade nuclear demagnetization cryostat, the cooldown of the sample is performed in several consecutive steps. First the large copper nuclear stage is precooled in the high 9 T magnetic field with the dilution refrigerator. It takes 50 (80) h to reach a nuclear and lattice temperature of 11 (9) mK at the first stage. After the precool the nuclear stage is thermally disconnected from the dilution unit by a superconducting aluminum heat switch and the copper stage is demagnetized slowly in 8 h, to maintain adiabaticity, to a low field of $40 - 80$ mT. The adiabatic demagnetization cools the nuclei, which in turn cool the lattice and a final electronic temperature of typically $50 - 100$ μK is reached. Before completing the first stage demagnetization, the second polarizing magnet of 7.5 T around the sample is magnetized in 2 h. However, we typically used only a 7 T field, as the second magnet is fixed to the still of the dilution unit, inside the vacuum can of the cryostat, and some safety margin was considered appropriate. The large nuclear heat capacity of the copper stage is then used as a thermal reservoir to cool down the sample spins. In high magnetic field, the polarization of spin-1/2 nuclei follows the simple relation [19]

$$p = p_{\mathrm{eq}}(1 - e^{-t/\tau_1}), \tag{2.1}$$

where the equilibrium polarization is

$$p_{\mathrm{eq}} = \tanh\left(\frac{T_z}{T_e}\right), \tag{2.2}$$

with the characteristic Zeeman temperature $T_z = \mu B/k_B$ ($T_z = 225$ μK in 7 T for Rh). The time constant of the exponential relaxation towards the equilibrium value is

$$\tau_1 = \frac{\kappa}{T_z}\tanh\left(\frac{T_z}{T_e}\right), \tag{2.3}$$

where κ is the high field Korringa constant for rhodium; $\kappa = 8.0$ sK (see Section 3.2.1). At low and intermediate fields, below ~ 0.5 T, $T_z \ll T_e$ and Eq. (2.3) reduces to the Korringa law, $\tau_1 = \kappa/T_e$. At 100 μK and 7 T, Eq. (2.3) gives a τ_1 of 9.7 h for Rh.

Practically the maximal polarization is reached in $50 - 70$ h, depending on the lattice temperature. Subsequently, the sample is demagnetized in about 2 h to zero field, cooling the spin system to temperatures below 1 nK. The lattice temperature of the sample remains at the temperature of the copper stage because of the solid thermal link between the stages. As the spin-lattice relaxation at these temperatures is very slow (for our sample $\tau_1 \approx 4$ h at 100 μK at zero field), the Rh nuclei remain cold for several hours, thus leaving enough time to perform a set of measurements.

Due to the large heat capacity of the copper nuclear stage the polarization cycle of the sample can be repeated $2 - 4$ times before a new precool of the first stage is required. Thus a set of experiments can be performed on the average every 3 or 4 days.

The lattice temperatures of the nuclear stages were measured by a pulsed Pt-NMR-thermometer [11] fixed to the top flange of the copper stage. The Pt-thermometer was calibrated at mK-temperatures against a primary ^{60}Co nuclear orientation thermometer and a commercial germanium-resistor thermometer. The accuracy of the Pt-thermometer was estimated to be better than 10% (see Section 3.2.1).

2.2.1 Negative spin temperatures

Negative polarizations or spin temperatures can be achieved by inverting the populations of the nuclear Zeeman levels. Such an inversion is best accomplished by reversal of a small external magnetic field in a time much shorter than the spin-spin relaxation time τ_2 of the nuclei [20,4]. τ_2 of rhodium is 10 ms [8] and thus a field reversal in about 1 ms is sufficient.

Our flipping efficiency $|p_f/p_i|$ was rather insensitive to the flipping field value and a field of 400 μT was used in most cases. On the other hand the efficiency was strongly reduced towards higher initial polarization. At $p_i = 0.3$, 83% of the initial polarization was conserved, but at $p_i = 0.8$ the efficiency had dropped to 60%. The rather large flipping losses can be explained by the severe eddy current screening, due to the bulkiness of our single crystal sample.

2.3 SQUID NMR setup

The measurements were done by SQUID NMR at low frequencies, between 3 and 1000 Hz. Two different coil systems were used during the course of the experiments.

The first coil system was wound solely with superconducting wires, consisting

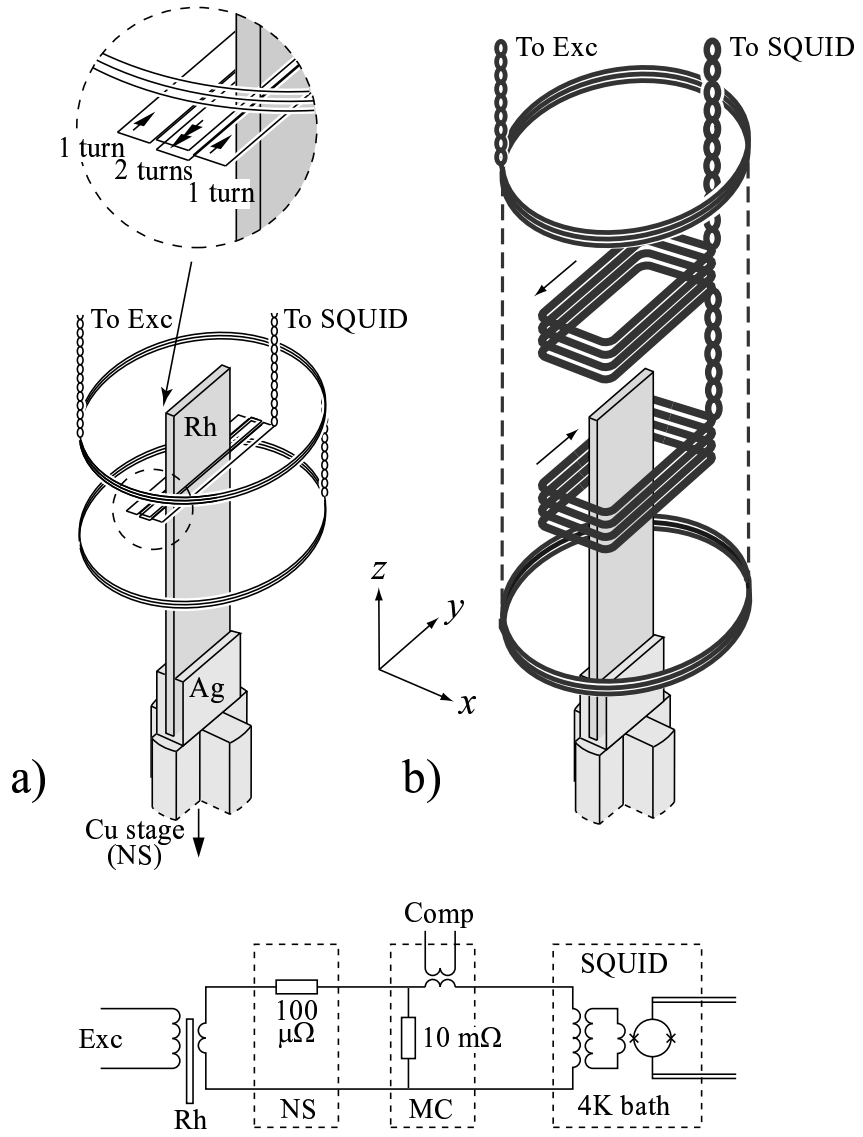

Fig. 1. The two coil arrangements used in the measurements. Part a) shows the superconducting pick-up coil setup used in the first set of the experiments, while part b) shows the Cu-wire coil system used for the latter set of the measurements. The figure is drawn approximately to scale. The bottom part of the figure displays the connection scheme to the SQUID. See text for details.

of the pick-up, excitation and x, y, z-static coils. The pick-up coil was a planar second-order gradiometer wound from 50 μm multifilamentary wire in a Cu-Ni matrix. The pick-up had two loops around the sample and single compensation loops of the opposite polarity on both sides of the sample, see part a) of Fig. 1. Such a pick-up loop could be placed very close to the sample giving a good filling factor, as a weak touch through the thin superconducting wire is not harmful. Moreover this geometry has the advantage that it eliminates both uniform and gradient disturbances. The excitation coil was a Helmholtz pair with 5+5 turns wound also of the 50 μm wire. The pick-up and excitation coils

were fixed by a glassfiber holder inside the radiation shield at mixing-chamber temperature. The static coils were placed outside the shield, two saddle coils for the x- and y-directions with $20 + 20$ turns each, and a straight solenoid for the z-direction with 110 turns. All coils were wound of 50 μm wire.

The pick-up coil was connected to an Oxford Instruments dc-SQUID [21], through the circuit shown in the lower part of Fig. 1. The circuit had a series resistance of ~ 100 $\mu\Omega$ and a shunt resistor of ~ 10 mΩ to give a bandwidth from about 15 Hz up to 3 kHz. Additionally the circuit was coupled to a compensation loop, which was used to monitor the gain of the SQUID. The series resistance was thermally anchored to the Cu nuclear stage to keep the generated thermal noise current to a minimum. The inductance of the pick-up loop was estimated to be 0.12 μH and the twisted-pair wiring up to the SQUID added about 1 μH, whereas the input inductance of the SQUID was 0.7 μH. The matching was thus not ideal, but the performance of the setup was satisfactory. Despite the cut-off frequency of about 15 Hz, measurements could well be carried out at 3 Hz, i.e., essentially in the static limit for Rh.

The second coil system employed mostly normal Cu-wire to circumvent the problems encountered with trapped flux of the order of a few μT in the superconducting coil system (see Section 3.9). The superconducting saddle coils for x- and y-directions were left intact to allow NMR at $B \gg B_{\rm loc}$, and all the other coils were replaced. To maintain the high-pass frequency of the pick-up loop around 100 Hz at the inductance level of about 1 μH, the resistance of the pick-up loop had to be less than 1 mΩ. Therefore a rather thick wire had to be used. The pick-up coil was wound of 0.5 mm Cu-wire as an axial astatic pair with $4 + 4$ turns, see part b) of Fig. 1. The pick-up loop with the connecting wire had a room temperature resistance of about 80 mΩ and an RRR of 100, giving a low temperature resistance of ≈ 0.8 mΩ. The excitation coil was a straight solenoid from 0.28 mm Cu-wire with two layers and 300 turns and the static z-coil was an end-compensated solenoid with 2 layers and 270 turns of the same wire. The maximum operating field of the Cu-wire z-coil was limited to about 150 μT, because of the Ohmic heating to the mixing chamber.

The resistive pick-up was connected to a different dc-SQUID from VTT [22], due to an untimely demise of the Oxford dc-SQUID. The same resistor circuit for the pick-up loop was utilized. Although the series resistor was not needed for the Cu-wire pick-up, its removal was unnecessary. The bandwidth of the pick-up loop was from about 100 Hz up to a few kHz. Even though the cut-off frequency was somewhat higher, a reasonable signal level could still be maintained down to 3 Hz.

The Cu-wire pick-up was used only for experiments in the superconducting state (Section 3.9), in all other measurements the superconducting pick-up system was employed.

The output of the SQUID was fed to an Ithaco 5610B lock-in amplifier to separate the components of the dynamical susceptibility $\chi(f, B) = \chi'(f, B) - i\chi''(f, B)$. The data were recorded with an HP34970A data-acquisition unit connected to a PC through an optical GPIB-cable. The signal generator was an HP3325B controlled by the PC.

3 Measurements

3.1 Continuous wave NMR

The primary measured data in these experiments consist of the NMR peaks in a small external field of typically around 300 μT (corresponding to 400 Hz) and very low frequency response at 3 Hz at zero external field to monitor essentially the static susceptibility. Additionally some NMR lineshapes were measured also in zero external field, where the absorption maximum is at about 50 Hz for rhodium.

In an external field, the NMR lineshapes were measured by sweeping the field while keeping the excitation frequency constant. The advantages, as compared to sweeping the frequency, were that a noiseless frequency could be chosen for the excitation and corrections because of the frequency dependent amplification and skin depth were not needed. We chose a measuring frequency of $f_{\mathrm{exc}} = 431$ Hz, which corresponds to a resonance field value of 320 μT for rhodium. The excitation amplitude was typically 5 nT, which was verified to be small enough not to deplete the nuclear polarization while sweeping through the resonance. The static external field was usually in the y-direction. One spectrum was typically measured in 2 minutes by sweeping the field between 200 and 440 μT.

The spectra were fitted to Lorentzian lineshapes with a free phase factor plus a background. The area of the absorption signal was deduced from the fit parameters.

The low frequency signal at 3 Hz was well below the zero field absorption maximum of Rh nuclei and was to a good approximation purely dispersive, $\chi(3\ \mathrm{Hz}) \approx \chi'(0)$. Consequently a rather high excitation amplitude, typically 160 nT, could be used without heating up the spin system.

3.2 Spin lattice relaxation

The spin lattice relaxation time τ_1 has a major role in nuclear cooling experiments, as it defines the characteristic timescale of the measurements. If the relaxation is too fast, the spin system must be cooled in thermal equilibrium with the lattice, restricting the achievable temperatures to the microkelvin regime. Vice versa, with very long relaxation times, high initial polarizations become virtually inaccessible.

The spin lattice relaxation at low magnetic fields also reflects the sample purity. Theoretically the relaxation should be $2-3$ times faster at zero field as compared to high fields, $B \gg B_{\mathrm{loc}}$ [23]. Paramagnetic impurities in the sample, however, speed up the relaxation at low fields up to several orders of magnitude, see e.g. [1].

3.2.1 τ_1 at intermediate fields

The spin-lattice relaxation time τ_1 in metals is obtained from the Korringa law (except at very high fields, see Eq. (2.3)),

$$\tau_1 = \kappa/T_e, \tag{3.1}$$

where κ is the Korringa constant. The equation is valid for magnetic fields much higher than B_{loc}.

We measured the spin-lattice relaxation time at a field of 100 mT, where the condition $B \gg B_{\mathrm{loc}}$ is safely satisfied. However, as SQUID-NMR measurements could not be performed at this field, the relaxation was measured by the conventional field cycling technique. The polarization is first defined in the typical measurement fields of $B \approx 300$ μT by measuring several spectra and fitting them to an exponential decay. The external field is then adiabatically, in about 60 s, swept to 100 mT and persisted for $2-3$ h to obtain a sufficiently large change in polarization. The field is then swept back to the low value and several spectra are measured. The relaxation time during the high field period can then be interpolated from the values before and after, by assuming exponential decay. The spin-lattice relaxation time is plotted in Fig. 2 at different electronic temperatures. In 100 mT, the equilibrium polarization is still insignificant at these temperatures and assumed to be zero. A linear fit gives the Korringa constant $\kappa = 8.0 \pm 0.1$ sK, while Narath *et al.* [8] have given the value $\kappa = 10 \pm 2$ sK.

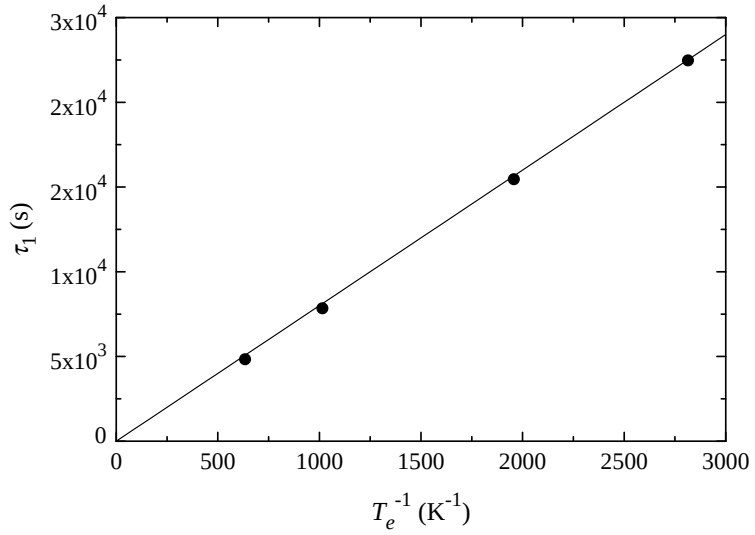

Fig. 2. The measured spin-lattice relaxation time at an intermediate field (100 mT) vs. the inverse electronic temperature. The solid line is a linear fit to the data. The error limits are approximately of the size of the datapoints.

The measured Korringa constant was used for checking the temperature of the sample lattice at lower temperatures of the copper stage. The spin-lattice relaxation was consistent with the Korringa behavior down to the lowest temperatures displayed by the Pt-NMR thermometer, indicating that the thermal connection between the sample and the copper stage was good and that the heat leak to the sample was small. Based on this, the stated values of the sample lattice temperature are estimated to be accurate within ± 10 μK even at the lowest temperatures.

3.2.2 τ_1 at zero field

The reciprocal of the spin lattice relaxation time in $B = 0$ as a function of electronic temperature is shown in Fig. 3. As τ_1 in low fields depends on the nuclear polarization, the data have been extrapolated to the limit of $p = 0$. The behavior is fairly well linear, but the fitted line has an offset from origin, corresponding to an additional temperature independent term in the spin lattice relaxation, viz., $1/\tau_1(T) = 1/\tau_1^i + T/\kappa_0 = 1/(29 \times 10^3 \text{ s}) + T/(2.6 \text{ sK})$. The zero field Korringa value $\kappa_0 = 2.6$ sK $= \kappa/3.1$ agrees reasonably with theoretical expectation of $\kappa/\kappa_0 = 2 - 3$ [23]. The temperature independent term $1/\tau_1^i$ evidently arises from paramagnetic impurities in the sample.

As mentioned above, the relaxation time depended on nuclear polarization, decreasing by about 35% from zero polarization to $p = 0.8$. This agrees well with the p-dependence observed earlier by Vuorinen *et al.* [4]. The relaxation

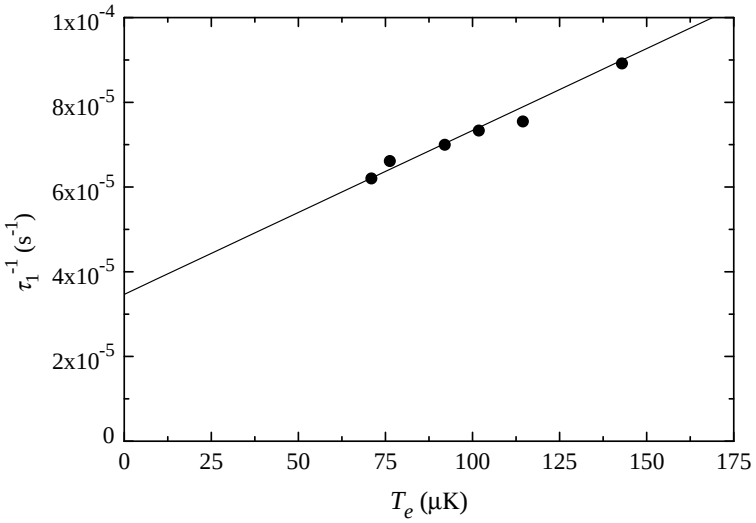

Fig. 3. The spin lattice relaxation rate, τ_1^{-1}, extrapolated to $p = 0$, as a function of electronic temperature. The error bars for the extrapolation have about the same size as the datapoints, whereas the error in the temperature scale is estimated to be ± 10 μK. The solid line is a linear fit to the data, see text for details.

was also $10-15\%$ slower at negative temperatures down to $p = -0.55$. This has been suggested to derive from an asymmetry in the energy spectrum induced by the exchange interaction [24].

3.3 Calibrations

3.3.1 p-calibration

In adiabatic nuclear cooling experiments the relevant measure of the thermodynamic state is the entropy S of the spins. For a spin-$\frac{1}{2}$ system, S per mole in an external field is a simple function of nuclear spin polarization p, viz.,

$$S/\mathcal{R} = \ln 2 - \tfrac{1}{2}[(1+p)\ln(1+p) + (1-p)\ln(1-p)], \tag{3.2}$$

where $\mathcal{R}$ is the gas constant. The measurement of p is rather straightforward, since at sufficiently high fields, $B \gg B_{\mathrm{loc}}$, the polarization is proportional to the area of the NMR absorption signal,

$$p = C \int_0^\infty \chi''(B) dB, \tag{3.3}$$

where C is a calibration constant.

The calibration constant C is determined as follows [25]: First an equilibrium polarization at high field (7 T) is produced at a relatively high electronic temperature (≈ 1 mK), where good thermal equilibrium can be assumed between the sample and the Pt-thermometer. Also the time constant of the spin-lattice relaxation at these temperatures is relatively short, around 2 h, so that an equilibrium situation is achieved in a reasonable time. Subsequently the nuclei are adiabatically demagnetized to a low measuring field ($\approx 300\ \mu$T), while the electronic temperature is kept constant. The polarization of the nuclear spin system in the high field can be obtained from Eq. (2.2) and when the relaxation rate is known the initial polarization at the end of the demagnetization can be calculated. A series of NMR spectra are measured, the area A_i under the absorption curve is determined from the spectra and an exponential decay fitted to the areas as a function of time. From the fit the area can be extrapolated back in time to the endpoint of the demagnetization, which gives the area A_i corresponding to the calculated initial polarization. To reduce the error margin, this procedure is repeated at several electronic temperatures and the final value of C is obtained from a linear fit. Our calibration is shown in Fig. 4.

Although the integrated response of the spin system is strictly proportional to the polarization, Eq. (3.3), over the whole range $p = -1...1$, the measured NMR signal from a metallic sample does not necessarily sustain this simple relation at all times. This is because of the eddy currents distorting the signal in a nontrivial manner at the highest polarizations, so that it is not correct simply to extrapolate beyond $p > 0.5$. Our analysis indicates that the maximum deviation from the linear relation for our sample is $10 - 15\%$ at $p = 1$. This effect will be discussed further in Section 3.4.

3.3.2 Local field

The local field B_{loc}, which becomes relevant in small external fields, describes the average magnitude of the fluctuating field at the nuclear position caused by spin-spin interactions. B_{loc} is defined as

$$B_{\mathrm{loc}}^2/B^2 = \mathrm{Tr}\{\mathcal{H}_{\mathrm{ss}}^2\}/\mathrm{Tr}\{\mathcal{H}_{\mathrm{Z}}^2\}, \tag{3.4}$$

where $\mathcal{H}_{\mathrm{ss}} = \mathcal{H}_{\mathrm{dip}} + \mathcal{H}_{\mathrm{ae}} + \mathcal{H}_{\mathrm{RK}}$ combines the mutual interaction terms.

One method for deducing B_{loc} is to measure the field dependence of the adiabatic susceptibility. The longitudinal and transverse susceptibilities are related

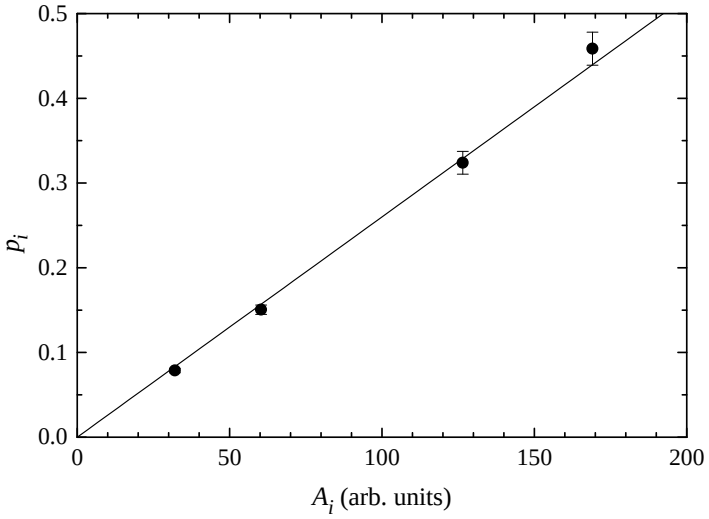

Fig. 4. Calculated p_i vs. the initial area A_i under the absorption spectra at 431 Hz. The points are measured at different electronic temperatures between 0.35 and 1.6 mK. The solid line is a linear fit to the data. The error estimates for the initial areas are smaller than the point size.

to each other by [26]

$$\chi_{\parallel} \approx \frac{\chi_{\perp}}{1 + B^2/B_{\rm loc}^2}. \tag{3.5}$$

At the high-T limit the Curie law $\chi_{\perp} = C/T$ is valid, while the field dependence of the final temperature is given by $T_f = (T_i/B_i)(B_f^2 + B_{\rm loc}^2)^{1/2}$. Equation (3.5) thus leads to

$$\chi_{\parallel} \propto (1 + B^2/B_{\rm loc}^2)^{-3/2}. \tag{3.6}$$

A measurement of the longitudinal susceptibility is shown in Fig. 5, where a function of the form of Eq. (3.6) is fitted. The value of the local field as well as the remanence field, which corresponds to the offset of the curve from $B_z = 0$, are obtained from the fit parameters. For improved accuracy several curves were measured with varying polarization and the local field value was taken from the extrapolation to the limit of zero polarization. This gave a value of $B_{\rm loc} = 33 \pm 2$ μT, which agrees very well with $B_{\rm loc} = 34$ μT adopted earlier by Hakonen *et. al.* [6]. The average remanence field value was 4.5 μT.

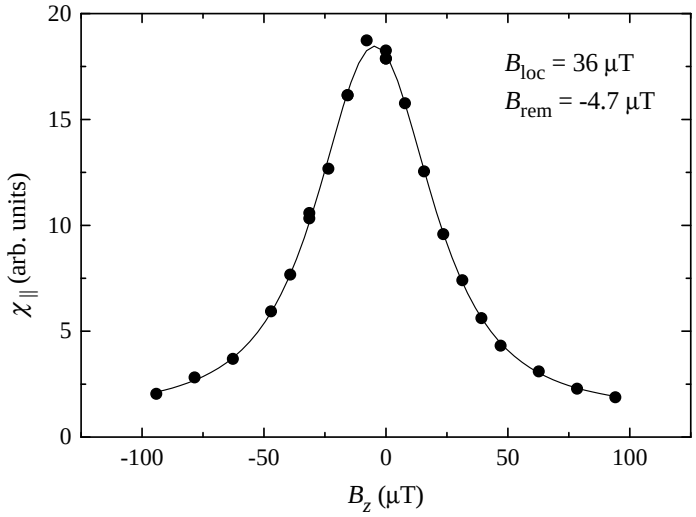

Fig. 5. A typical local field measurement, $\chi_{\parallel}$ is plotted as a function of the external magnetic field. The fitted line gives the local ($B_{\rm loc}$) and remanence ($B_{\rm rem}$) fields. The values obtained for this particular measurement are shown in the figure. The polarization during the measurement was $p \approx 0.26$.

3.3.3 χ-calibration

The absolute scale of the susceptibility is needed for the analysis of many of the measurements. Earlier the absolute value has been deduced by using the relation between $\chi'(0)$ and the magnetization of the spin system at intermediate fields [1]. This method is, however, not well suited for our sample, because of the strong eddy current effects, which distort this dependence.

Obviously the most reliable scale could instead be obtained from the signal level in the superconducting state, where $\chi'(0) = -1$. This scale was reproduced very well in several cooldowns, indicating that the sample most probably was fully in the Meissner state.

The consistency of the absolute scale was verified by other methods of calibration. An absolute value could be deduced by measuring the high frequency response of the pick-up coil with and without the sample, since at high enough frequencies, $f > 1000$ Hz, the susceptibility of the sample is practically -1 due to almost complete eddy current screening. The inferred value, although less accurate, agreed within 20% with the scale from the sc-transition. An other estimate was obtained from the measurement of the temperature scale, see Section 3.5. The mismatch was also within some 20%.

The eddy currents induced in the conducting sample evidently affect the NMR signal. In ordinary NMR experiments the nuclear magnetization is small and thus the permeability of the sample is essentially that of vacuum, $\mu \approx \mu_0$. Under this condition the eddy currents only cause a phase shift and an overall reduction of the signal amplitude, even if the skin depth δ is comparable to or less than the sample thickness d. The shape of the phase corrected NMR line remains intact.

In the case of highly polarized nuclei, the situation is essentially different. The skin depth is defined as

$$\delta = \frac{1}{\mathrm{Im}\sqrt{\mathrm{i}\omega\sigma\mu_0\mu_\mathrm{r}}}, \tag{3.7}$$

where σ is the electrical conductivity and $\mu_r = 1 + \chi$ is a complex valued field and frequency dependent relative permeability. When $|\chi|$ at the magnetic resonance is not vanishingly small compared to 1, its influence on δ can not be omitted, in particular if $\delta \sim d$. In our sample at $p = 0$ ($\chi = 0$), the skin depth is equal to the thickness already at about 100 Hz, whereas the typical measurement frequency is 431 Hz. At the highest nuclear polarizations in our sample, the skin depth does vary notably as the static field is swept through the resonance although a constant frequency is used. This causes nontrivial deviations from the genuine shape of the NMR signal. These effects were studied by a phenomenological model based on the Bloch equations and classical electromagnetism [27].

In the framework of this model the shape of the NMR spectra could be calculated with and without including the effect of eddy currents. Noticeable changes in the position and width of the NMR absorption peaks result. Furthermore, the dependence of the area of the absorption signal on polarization is no longer linear, but deviates slightly at high polarizations, as illustrated in Fig. 6. The polarization values based on the Lorentzian fits and the linear area dependence have been corrected accordingly.

The corrected polarization values are somewhat larger than those obtained from the simple linear extrapolation. Based on the linear scale the best ratings were $p = 0.86$ on the positive side and $p = -0.49$ on the negative side. Taking into account the eddy current correction, the highest polarizations achieved were $p = 0.95 \pm 0.03$ and $p = -0.55 \pm 0.03$. The corrected scale gives much better agreement with the expected behavior, as the initial conditions, $B = 7$ T and $T_e < 100$ μK, yield the calculated polarization values $p \approx 0.99$ and the

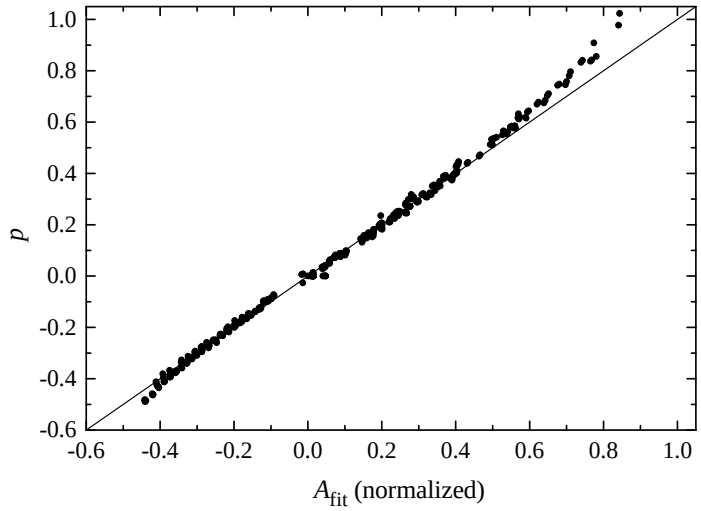

Fig. 6. The eddy current corrected polarization values as a function of the normalized area of the Lorentzian fits. The solid line with slope 1 is plotted for reference.

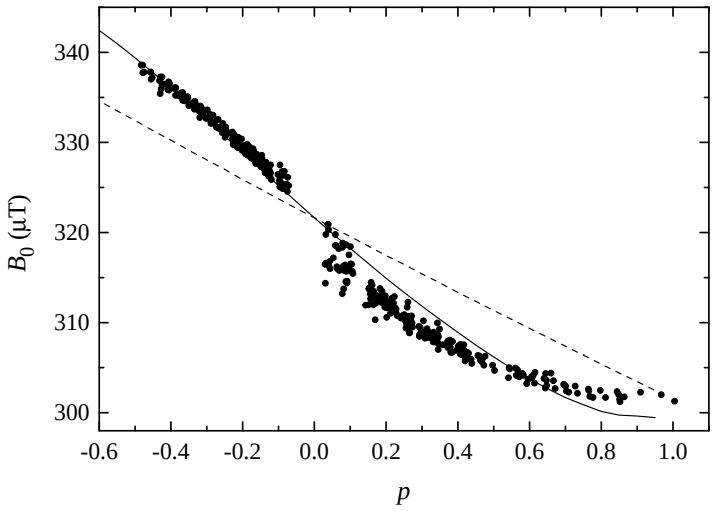

Fig. 7. Peak position B_0 of the NMR absorption signal as a function of polarization. The solid and dashed lines show the calculated behavior with and without the eddy current effects, respectively. The peak position of a spectrum was deduced by fitting a parabola to a narrow section around the maximum of the signal.

losses during the demagnetization from 7 T down to the low NMR-measuring field are only a few percent even for pessimistic assumptions. Throughout the succeeding sections the corrected polarization scale is used.

The model also reproduces very well the position and width of the NMR

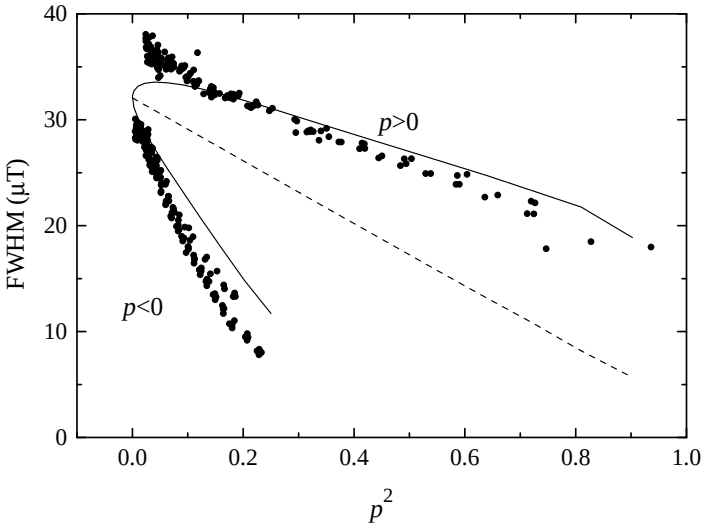

Fig. 8. The full width at half maximum (FWHM) of the NMR absorption peak as a function of polarization squared. The upper branch corresponds to spectra measured at positive polarizations and the lower branch to spectra with negative polarizations. The solid and dashed lines show the calculated behavior with and without the eddy current effects, respectively. The expected behavior without the eddy current effects, the dashed line, is identical for both positive and negative polarizations. The clear asymmetry in the measured data between $p < 0$ and $p > 0$ is caused by the eddy currents.

absorption peak. The peak positions of the measured data are shown in Fig. 7 as a function of polarization along with the calculated behavior both with and without the eddy current effects. Similarly in Fig. 8 the full width at half maximum as a function of p^2 is plotted and compared with the calculations. Note in particular, that the pronounced difference in the data between $p < 0$ and $p > 0$ is nicely explained by the constructed model, in contrast to the situation without the eddy currents.

3.5 Spin temperature at $B = 0$

Although the entropy S or the polarization p are more relevant measures of the thermodynamic state of the spin system, the nuclear temperature T is, nevertheless, a more familiar parameter. The determination of the temperature scale also provides easier comparison with other experiments and theoretical models.

As the nuclei of the rhodium sample are not in thermal equilibrium with the conduction electron system, the nuclear spin temperature cannot be measured by means of an external thermometer. Therefore the spin temperature is de-

duced directly from the second law of thermodynamics

$$T = \Delta Q / \Delta S, \tag{3.8}$$

i.e., the spins are heated by a known amount ΔQ and the resulting entropy change ΔS is measured. The heat pulse can be given by NMR absorption and the absorbed energy per mole is

$$\Delta Q = \pi f \chi''(f) B_h^2 \Delta t V_m / \mu_0, \tag{3.9}$$

where $\chi''(f)$ is the absorption part of the complex susceptibility, B_h the amplitude of the excitation field $B_h \sin(2\pi f t)$, Δt the duration of the pulse and V_m the molar volume of Rh. In addition, for a spin-$\frac{1}{2}$ system in high fields the entropy per mole is a simple function of the polarization p, see Eq. (3.2).

In practice a temperature measurement is performed by first recording the nuclear polarization at $B \gg B_{\mathrm{loc}}$, typically at 300 μT, sweeping the field adiabatically to the desired value, usually zero, giving the heat pulse, ramping up the field again, and recording the polarization after the heat pulse. We used a heat pulse with an amplitude of 40 nT at a frequency of 42 Hz, which is below the limit of eddy current screening and close to the absorption maximum in zero field.

The exact magnitude of the excitation pulse amplitude B_h is difficult to calculate accurately, due to the induced eddy currents in the copper shield and other metallic parts around the coil system. Also the absolute value of the absorption at the frequency of the heating pulse is difficult to establish with high precision. To circumvent these problems the temperature scale can be adjusted by checking it against the second order $1/T$-expansion of entropy

$$S = \mathcal{R} \ln 2 - \lambda V_m (B^2 + B_{\mathrm{loc}}^2) / 2\mu_0 T^2, \tag{3.10}$$

which is valid at the high temperature limit. The zero-field temperature scale is shown in Fig. 9 together with this expansion. The independently estimated parameter values in Eq. (3.9) are consistent with the high temperature limit using $B_{\mathrm{loc}} = 33$ μT within a factor of 1.3.

A temperature measurement utilizing the second law of thermodynamics is rather tedious in practice and has the disadvantage that the lowest achieved

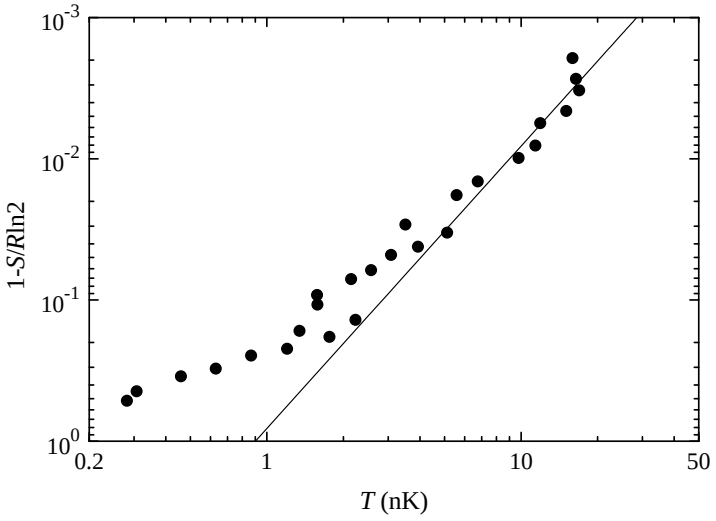

Fig. 9. Reduced entropy as a function of nuclear temperature in zero field. The solid line shows the high temperature expansion $1 - S/R\ln 2 \propto T^{-2}$, where the value $B_{\rm loc} = 33\ \mu$T is used.

temperatures can never be measured as the system must be heated to perform the measurement. By finding a relation between $T(B = 0)$ and $p(B = 320\ \mu\mathrm{T})$, the temperature measurement is considerably simplified, as the temperature can then be obtained from an easily measurable quantity. A simple candidate for such a relation can be derived by manipulating the different high temperature expansions of entropy [28], giving a semiempirical formula

$$|1/p| - 1 = b|T|, \tag{3.11}$$

where $b = (\mu_0 \mathcal{R}/\lambda V_m B_{\rm loc}^2)^{1/2} = 0.95\ \mathrm{nK}^{-1}$.

From the relation of Eq. (3.11) the nuclear spin temperature corresponding to the highest achieved polarization can be calculated, resulting in a minimum spin temperature $T < 100$ pK. It is pointless to state the lowest temperature more precisely than this, as the assumptions made along the way accumulate to an uncertainty of more than 50%.

3.6 Static susceptibility at $B = 0$

The measurement of the static susceptibility is relevant, as ordering of the nuclear spins should produce clearly observable modifications to this quantity.

The inverse of the static susceptibility also provides an easy comparison with the Curie-Weiss law.

Static susceptibility at $B = 0$ as a function of nuclear polarization (p measured at $B \sim 300$ μT) is shown in Fig. 10. This data were measured with the Cu-wire pick-up system because of the smaller remanence field. Further, the absolute value of the static susceptibility could be established more accurately for the Cu-wire pick-up from the signal level of the superconducting transition.

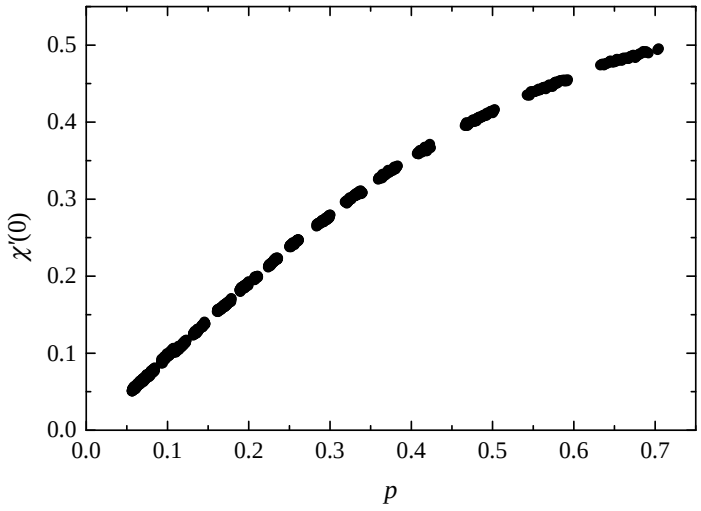

Fig. 10. Static susceptibility (in absolute units) as a function of nuclear polarization. During the gaps in the data, the polarization was measured at $B \sim 300$ μT.

The tendency of the ordering is seen clearly, when plotting the inverse absolute static susceptibility as a function of nuclear temperature, as in Fig. 11. The nuclear temperatures are measured with the method described in Section 3.5. The solid line in the figure is a fit of the antiferromagnetic Curie-Weiss law, Eq. (1.10), with θ as a free parameter. The fit gives the value $\theta = -1.6$ nK. Antiferromagnetic ordering should thus set in at a temperature of the order of 1 nK.

Signs of nuclear magnetic ordering in the Rh sample were looked for by monitoring the static susceptibility, or more precisely, the 3 Hz low-frequency response at high initial polarizations immediately after the demagnetization to low field. An antiferromagnetically ordered spin configuration should produce a plateau in the signal at the beginning, followed by a distinguishable kink when the order disappears [1]. The signal from a few of such runs is shown in Fig. 12 as a function of time from the end of the demagnetization. No anomalies attributable to magnetic ordering are observed; the signal is relaxing smoothly from the very beginning although the highest initial polarization was evidently as high as 0.95, where $S/R\ln 2 = 0.169$, i.e., only 17% of the

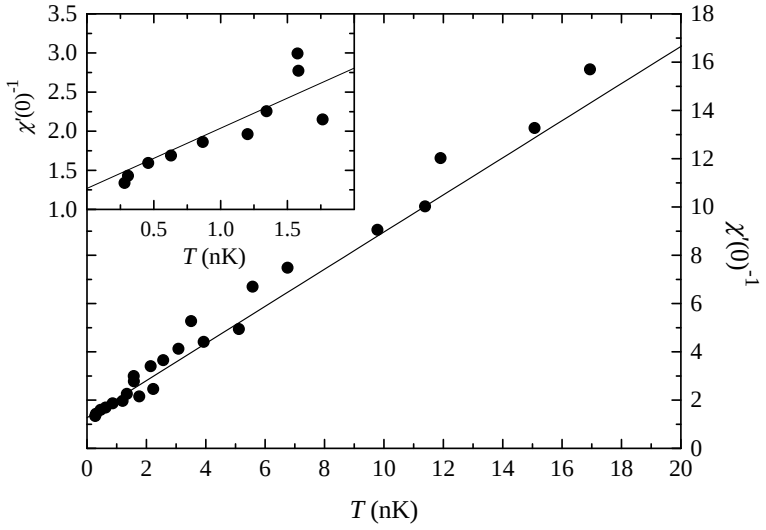

Fig. 11. Inverse static susceptibility vs. nuclear temperature. The solid line is a fit of the antiferromagnetic Curie-Weiss law with $\lambda = 1.3$ nK and $\theta = -1.6$ nK. The inset shows a magnification of the low temperature end.

entropy is left.

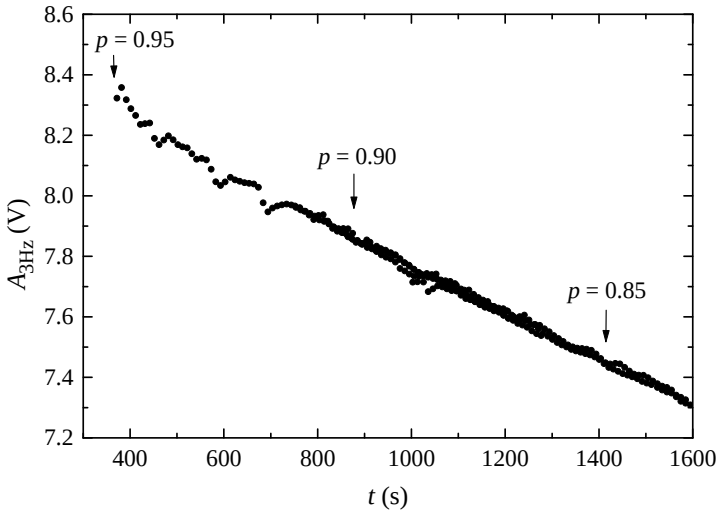

Fig. 12. Static susceptibility (in arbitrary units) as a function of time from the end of the demagnetization for runs with the highest initial polarization. The runs with lower initial polarization have been shifted in time to coincide with the best one.

The dipole-dipole interaction between the nuclei in solids allows one photon to flip two or more spins simultaneously, generating additional resonance lines at integer multiples of the Larmor frequency, $f_0 = \gamma B/2\pi$. These higher order resonances are of importance as their behavior provides direct information of the interactions between the spins. In particular, the frequency shift of the double-spin-flip peak can be used to deduce the strength of the isotropic indirect-exchange interaction [29,30].

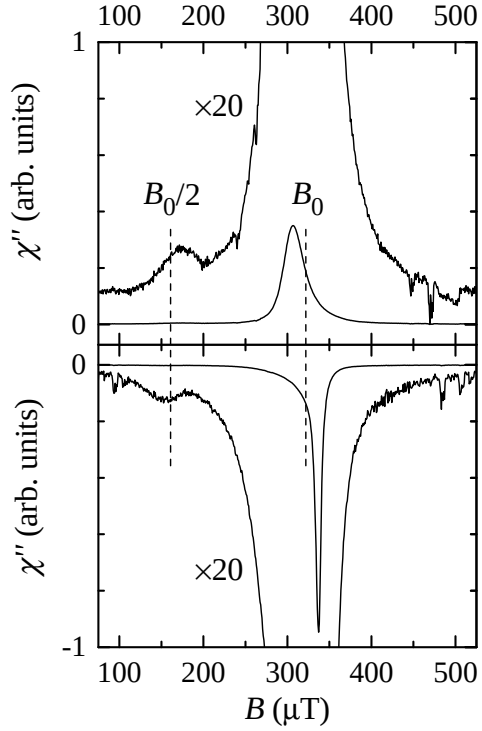

Fig. 13. Double-spin flip peak at $p = 0.39$ (top frame) and at $p = -0.39$ (bottom frame), with $f = 431$ Hz and orthogonal field NMR. The double-spin-flip satellite becomes clearly visible, when the data are magnified 20 times. The resonances are slightly shifted from the exact Larmor and double-Larmor positions.

We observed the double-spin process in rhodium at both positive and negative

temperatures, see Fig. 13. The details and results of the measurements were presented in Ref. [9]. In addition to the value of the R parameter, we obtained the effective gyromagnetic ratio $\gamma_{\rm eff}/\gamma = 1.18 \pm 0.04$, which agrees very well with the 16% correction employed earlier by Hakonen *et al.* [6] based on the measured NMR linewidths [8].

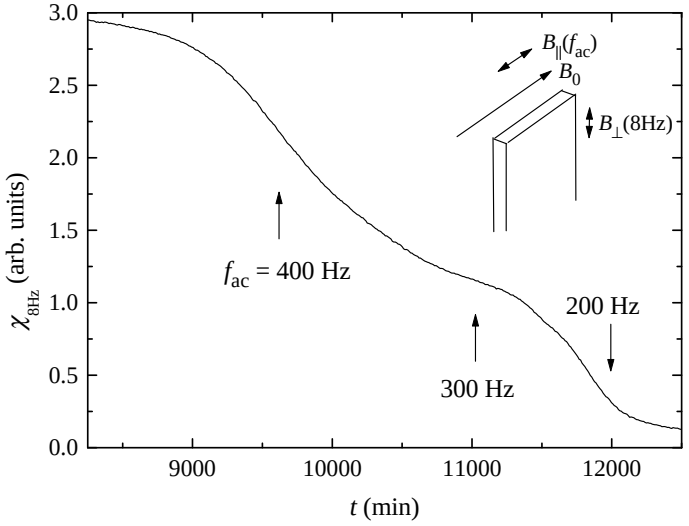

Fig. 14. Typical raw-data from a double-excitation measurement with the parallel field NMR geometry. The low frequency response is plotted as a function of time. Additionally the different field directions are shown with respect to the sample. See text for details.

The use of a parallel-field NMR geometry, i.e., applying the excitation and static fields parallel to each other, is much more sensitive for observing multiple spin-flips than a usual orthogonal-field NMR geometry. In the parallel-field geometry the primary Larmor resonance also arises due to the dipolar coupling and thus has an intensity comparable with the double-spin-flip peak [31,32]. We used a double-excitation method for detecting the parallel resonances, where the decay of a perpendicular low-frequency signal at 8 Hz, which essentially corresponds to polarization, was monitored during a slow frequency sweep of an ac-excitation $B_\parallel$ on top of the static field B_0. The low-frequency signal was excited by a small ac-amplitude of $B_\perp = 160$ nT perpendicular to the static field. The other excitation $B_\parallel$ parallel to the static field was tuned to a suitably large amplitude of 2.5 μT to cause a sufficiently rapid decay of polarization at the absorption maxima of the resonances. Longitudinal absorption can thus be calculated as $({\rm d}\chi_{8\rm Hz}/{\rm d}t)/\chi_{8\rm Hz}$. Figure 14 shows a typical raw signal, while the obtained longitudinal absorption is displayed in Fig. 15.

In Fig. 16 we present the evidence for a triple-spin-flip peak resonance. The amplitude of this process was considerably smaller than expected [31]. The static field value of 135 μT in the measurement of Fig. 16 is about the best

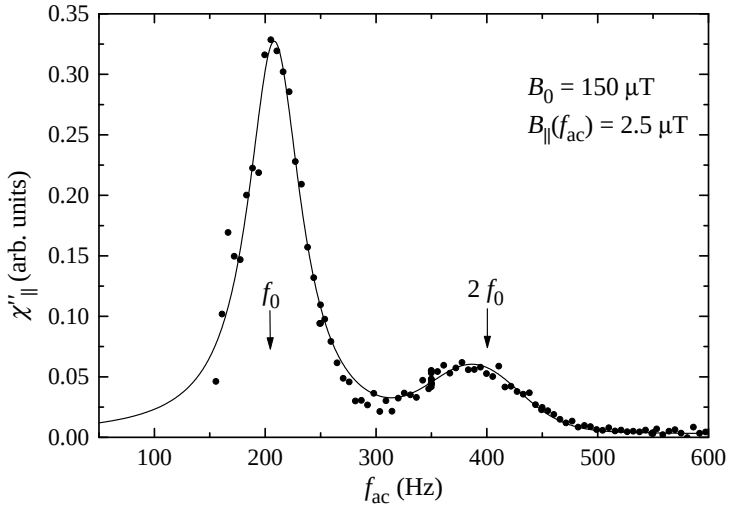

Fig. 15. Parallel field absorption in 150 μT showing the Larmor and double-spin-flip resonances. The data is obtained from the raw signal of Fig. 14. The pure Larmor and double-Larmor positions of the resonance lines are marked by f_0 and $2f_0$. The solid line shows a fit with a Lorentzian lineshape for the main peak and a Gaussian for the double-flip peak.

possible compromise for detecting this extremely weak feature. At higher field values the triple-spin-flip intensity decreases too much, behaving as $\propto B^{-4}$, whereas at lower fields the increasing overlap of the triple and double-spin-flip peaks prevents the separation of the two lines.

3.8 Resonances at parallel excitation

Field sweeps were performed also with the parallel excitation scheme, where the static field and the excitation were both along the y-axis (see Fig. 1). The excitation amplitude was 0.5 μT at a fixed frequency, while the static field was swept over the resonance in 8 minutes. The result of these sweeps was somewhat surprising, showing a double peak structure, where at high polarizations a sharp negative dip appeared on top of the resonance. A series of such sweeps with a measurement frequency of $f_0 = 591$ Hz are shown in Fig. 17 with decreasing polarization. The dip is very pronounced at high polarizations and disappears completely at low polarizations. This structure was clearly observable at measurement frequencies from 300 to 1000 Hz, becoming weaker as the frequency was lowered.

For a more quantitative analysis, such parallel resonances were fitted with a sum of two Lorentzian lineshapes, one with positive and the other with

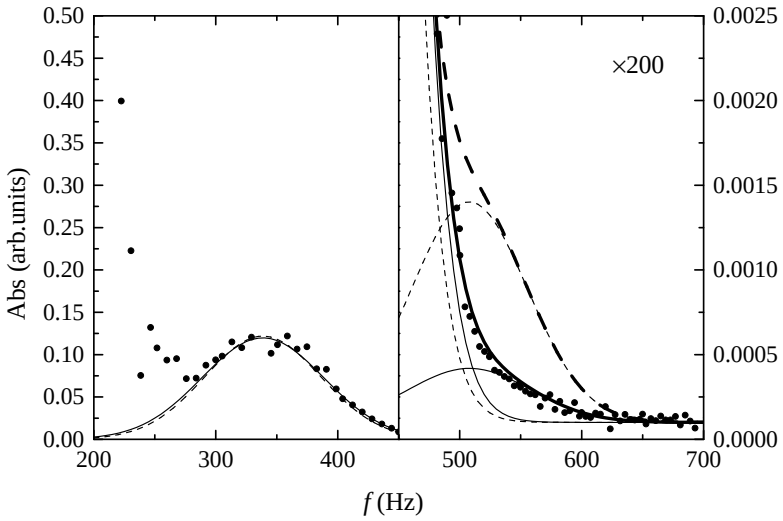

Fig. 16. Double and triple-spin-flip peaks at the field of 135 μT. The left side shows the double-spin-flip peak, while the right side displays its tail enlarged by a factor of 200. The solid lines present the fitted Gaussian shapes of the peaks. In the right side of the figure the two thin solid lines show the separated contributions of the double and triple-spin-flip peaks, whereas the thick solid line is the sum of the two. Respectively the dashed lines present the lineshapes calculated with the theoretically expected intensity of the triple-spin-flip peak. The data thus suggests a presence of the triple-flip peak at the tail of the double-spin resonance, but the intensity is about 3 times smaller than expected. The excitation amplitude was varied during the measurement for achieving better accuracy at the tail.

negative amplitude and with a common phase and background. An example of such a fit is shown in Fig. 18. The areas under the absorption parts of the two peaks can be deduced from the fit parameters and they are plotted in Fig. 19 as a function of nuclear polarization. The data can be fitted well with a power law, $a \cdot p^b$, giving $40.9 \cdot p^{1.21}$ for the wide peak and $27.5 \cdot p^{2.19}$ for the narrow opposite peak, respectively. The wide base peak is thus decaying nearly linearly with polarization, as may be expected, whereas the sharp dip has a much stronger p-dependence.

The mechanism producing such double-peak structures is not understood. The amplitude of the signal is much larger than expected for just a dipolar-coupling induced parallel resonance, which means that the orientation of the magnetic field must oscillate in addition to its amplitude. The observed structure cannot be explained merely by geometrical or eddy current effects, as in such a case the shape of the signal should remain the same independent of the polarization.

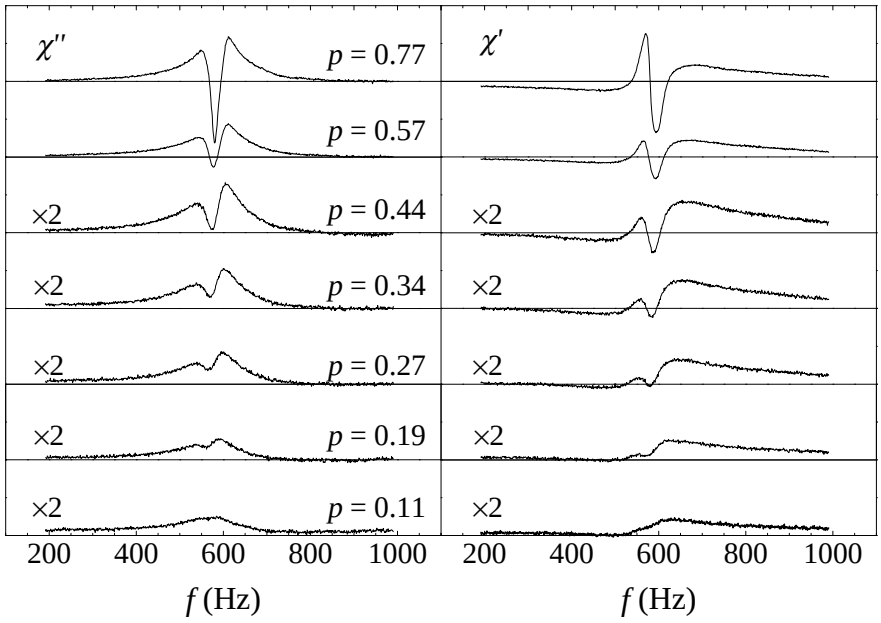

Fig. 17. Resonance curves measured with the parallel excitation scheme at $f_0 = 591$ Hz with varying polarization. The two columns show the absorption and dispersion parts. The lowest 5 spectra are magnified by a factor of 2. Polarization values were deduced by measuring spectra with the conventional NMR-scheme in between.

3.9 Superconducting rhodium

3.9.1 The superconducting transition

Rhodium is a type-I superconductor with the lowest known T_c of pure elements, 325 μK [5]. The critical field B_c is also extremely small, 4.9 μT, and supercooling is known to be strong, making the transition very difficult to achieve experimentally.

We searched for the transition first by using the superconducting pick-up coil system of Fig. 1 a, but the transition was not detected. As this was done before magnetizing the second polarizing coil surrounding the sample for the first time after the cooldown, the problem was most probably originating from trapped flux in the superconducting pick-up coils inside the magnetic shielding and close to the sample. Thus in later experiments a Cu-wire pick-up coil system (see Section 2.3) was installed to reduce such problems.

With the resistive pick-up system the superconducting state of Rh was de-

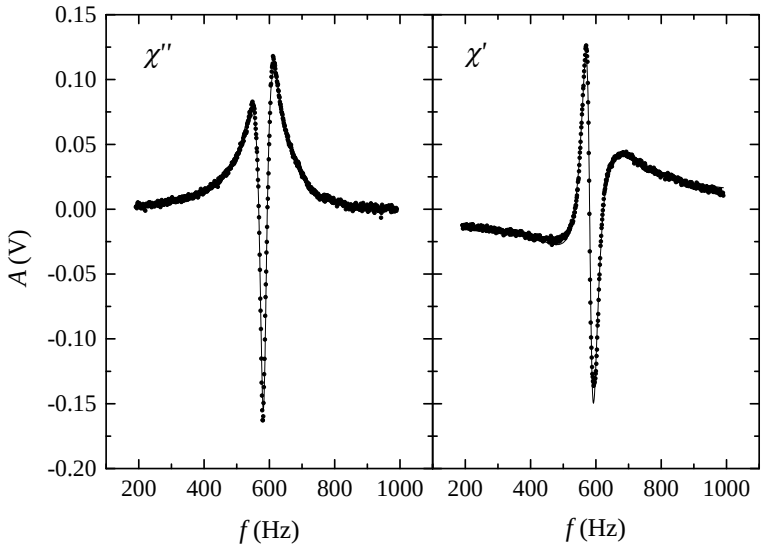

Fig. 18. The first resonance curve of Fig. 17 fitted with a sum of two Lorentzian lineshapes with opposite signs. Both the absorption and dispersion parts are shown.

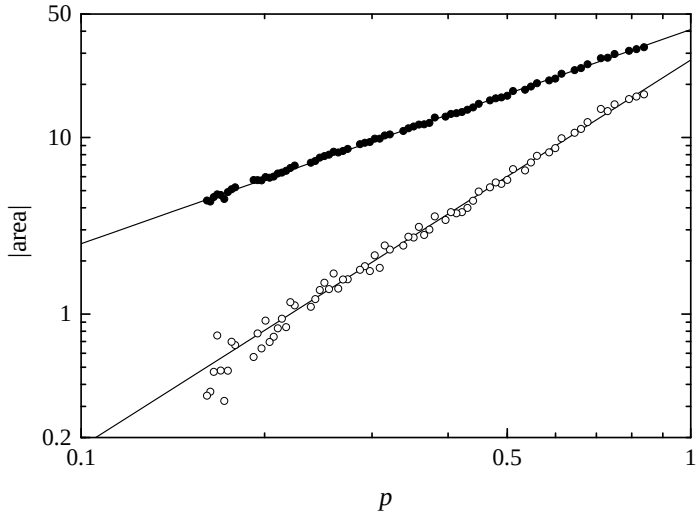

Fig. 19. Areas of the Lorentzian fits to the data of Fig. 17 as a function of polarization. The closed points correspond to the wide base peak whereas the open points correspond to the opposite dip. The solid lines show fits of the form $a \cdot p^b$, see text for details.

tected immediately. Typical traces of the transition are shown in Fig. 20; an excitation frequency of 431 Hz with an amplitude of 0.5 nT was used. Typically, the critical fields of the transition were measured by sweeping the z-direction static coil, but some traces were also recorded in the x-direction. The demagnetization factors are very different for these field directions, $D = 0.01$

for z-axis and 0.91 for the x-axis. In the x-direction sweeps the sample is thus expected to be in the intermediate state when $0.1 < B/B_c < 1$, but as seen in Fig. 20 such a state appears unstable and the sample returns quite early to the normal state. The y-direction coil was unfortunately broken in these cooldowns.

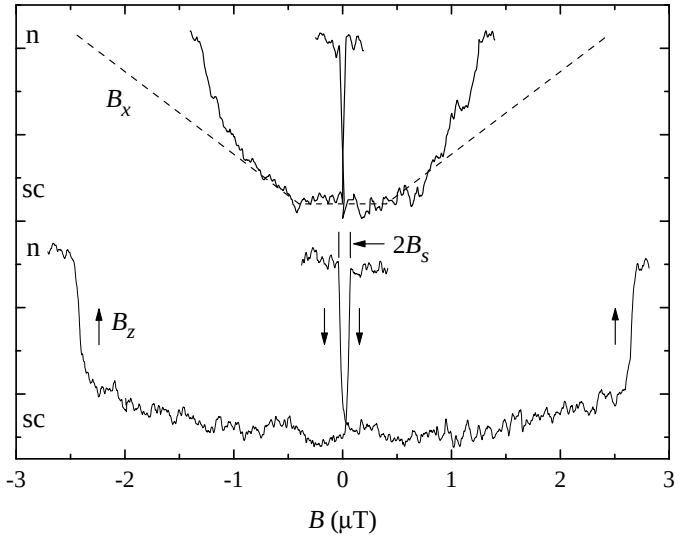

Fig. 20. Typical transition traces, measured at $T_e = 102$ μK. In the upper trace the field sweep was in the x-direction and in the lower one in the z-direction. The signal level of the upper trace has been shifted by +0.5 for clarity. The expected behavior with a wide intermediate state for the sweep in the x-direction is shown by the dashed lines. Note the very strong supercooling, when entering the superconducting state.

The lowest electronic temperature achieved was $T_e \approx 60$ μK, whereas the sc-transition could not be detected above 140 μK, owing to the strong supercooling. The temperature dependence of the measured critical field is shown in Fig. 21. It follows very well the usual dependence for type-I superconductors, $B_c(T_e)/B_c(0) = 1-(T_e/T_c)^2$, which is illustrated by the solid line. From the fit we obtain $B_c(0) = 3.4$ μT and $T_c = 210$ μK, which are somewhat lower values than reported by Buchal *et al.* [5]. It is not clear if this is caused by a larger concentration of paramagnetic impurities, as the starting material of our sample was rather similar to those of Buchal *et al.* As a contradicting indication, the residual resistivity ratio of our sample was higher, 740 as compared to 450.

The supercooling field B_s, see Fig. 20, is shown in the inset of Fig. 21 as a function of temperature. The discontinuities in $B_s(T_e)$ are not understood.

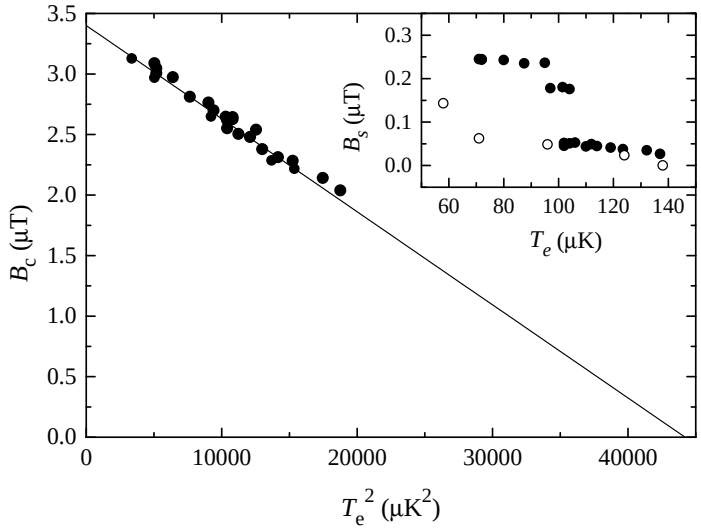

Fig. 21. Critical field as a function of temperature squared. The fitted line gives $B_c(0) = 3.4$ μT and $T_c = 210$ μK. The inset shows the supercooling field B_s as a function of temperature. The open and closed points are from two different cooldowns of the cryostat. All data are from sweeps in the z-direction.

3.9.2 Spin lattice relaxation in the superconducting state

Rhodium has a very rare property among the superconductors, that the critical field is much lower than the internal local field of the nuclei; $B_c \sim \frac{1}{10} B_{\mathrm{loc}}$. This is a necessary condition for being able to adiabatically switch between the normal and sc-states, without disturbing the nuclear spin system. This enables a simple measurement of the spin lattice relaxation time τ_1 in both the normal and sc-states and is essential if the effect of substantial nuclear magnetization is about to be examined.

For such measurements, the nuclei were polarized in a field of 2 T. Higher field values could not be applied because of the increasing remanence after demagnetization. Already from 2 T a particular degaussing cycle was required to reduce the remanence field below the very small supercooling field of the sc-transition. Nevertheless a polarizing field of 2 T allowed us to reach values of up to $p = 0.55$.

The spin lattice relaxation times were measured by monitoring the ac susceptibility at a frequency of 3 Hz. Of course in the sc-state the response of the nuclei could not be seen because of the Meissner effect. The sc-state spin lattice relaxation times were interpolated from the normal state values before and after a period in the sc-state, as shown in Fig. 22.

The relaxation rates are plotted in Fig. 23 in both the normal and sc-states as a

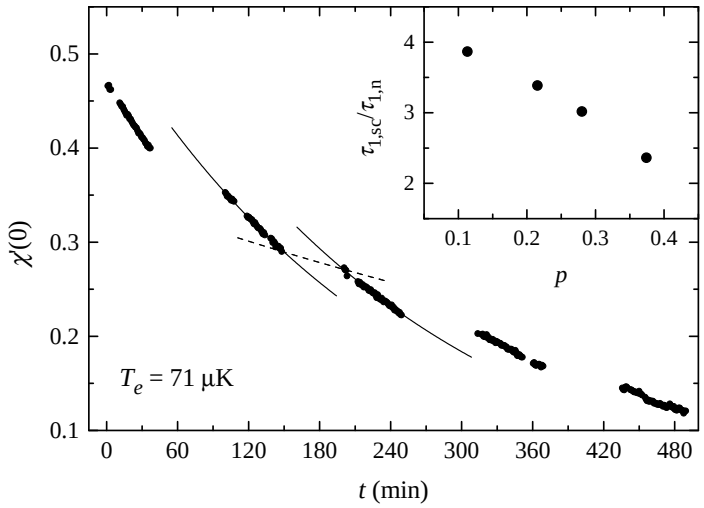

Fig. 22. Part of the data from a relaxation rate measurement at $T_e = 71$ μK and $p_i = 0.55$. The static susceptibility as a function of time is shown. The data are measured in the normal state, whereas during the large gaps the sample is in the superconducting state. The solid lines show exponential fits to the normal state data, while the dashed line shows the interpolation for the relaxation in the sc-state. The small gaps in the data are caused by unlocking of the dc-SQUID. The inset, where the ratio of the relaxation times is plotted as a function of static susceptibility, shows the data after the analysis. Note the strong $\chi'(0)$-dependence of the ratio.

function of electronic temperature. As the relaxation rate depends on nuclear polarization, the data are extrapolated to the limit $p = 0$. The relaxation rates can be directly compared, as the normal state data are measured in the supercooled phase, i.e. in practically zero field ($B \ll B_{\rm loc}$). The normal state values should display a linear behavior as dictated by the Korringa law (see Section 3.2.1), whereas the sc-state values well below T_c should show an exponential behavior, $\propto e^{-\Delta/k_B T}$, according to the BSC-theory. Close to T_c a coherence enhancement of $\tau_{1,\rm sc}$ is expected [33,34]. The sc-state data fit well the proposed exponential behavior, with $\Delta/k_B T_c = 0.79$, which is, however, about a factor of two smaller than the BCS value of 1.76. Further, the data does not indicate any coherence enhancement close to T_c. Note also that the offset observed in the normal state relaxation rate is completely suppressed in the sc-state.

Finite nuclear polarization reduced the ratio of the relaxation times in the normal and superconducting states, see the inset of Fig. 22. This is illustrated in Fig. 23 by the dashed curves obtained with $p = 0.5$. The relative change in the normal state relaxation is not very large, but the sc-state time constant is significantly modified. A more detailed account of these measurements and their analysis is presented in Ref. [35].

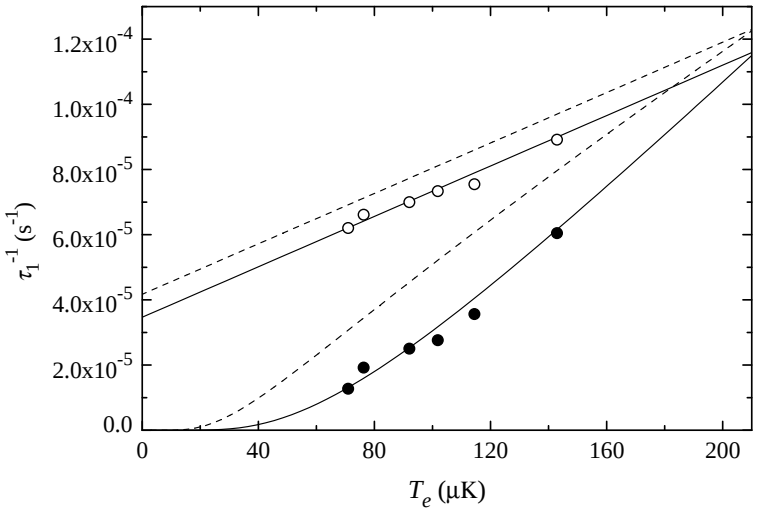

Fig. 23. The zero-field spin lattice relaxation rate in the normal (open points) and superconducting (closed points) states as a function of electronic temperature at the limit of zero nuclear polarization. The solid lines show a linear and an exponential fit to the data, whereas the dashed lines show the behavior at $p = 0.5$. For clarity the data points at finite nuclear polarizations are not shown.

3.9.3 Static nuclear magnetization and the superconducting transition

The nonzero nuclear magnetization affects the superconducting state, as it adds to the magnetic field inside the sample. The magnitude of this effect can be studied by measuring the critical field as a function of the nuclear static susceptibility at a constant electronic temperature. The result of such a measurement is shown in Fig. 24.

The expected behavior of the critical field can be deduced from the basic equations of electromagnetism leading to

$$B_c(\chi') = B_c(\chi' = 0)\frac{1 + D\chi'}{1 + \chi'}. \tag{3.12}$$

The demagnetization factor is $D = 0.01$, as the transitions were measured along the z-axis of the sample. The expected behavior is reproduced rather well, as seen in Fig. 24, although there is a small difference in the slope, which we cannot account for. Note that the magnetic field here is far less than able to align the randomly oriented nuclear magnetization: $M = \chi H \ll pM_{\mathrm{sat}}$ and at $B = 0$, $M = 0$.

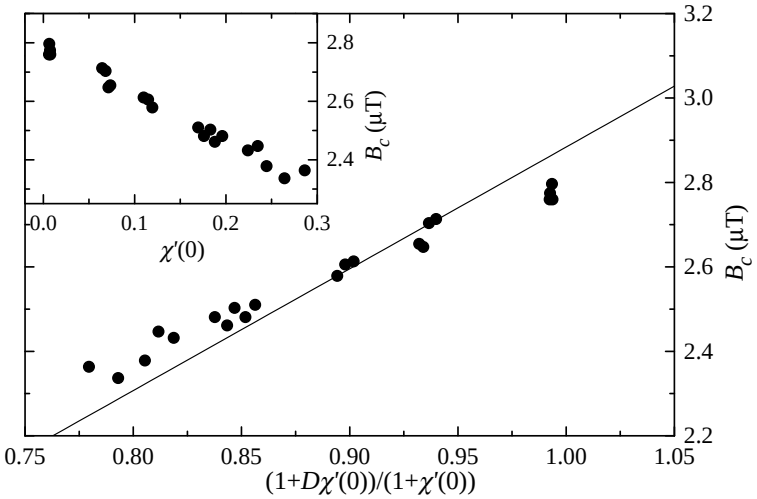

Fig. 24. The critical field of the superconducting transition as a function of nuclear static susceptibility. The x-axis was chosen so that the behavior should be linear and intersect the origin as shown by the solid line. The inset shows the data with linear scales. The electronic temperature during the measurement was 89 μK.

4 Conclusions

We have studied the nuclear spin system of rhodium by low frequency NMR at ultralow temperatures. Rhodium has spin $\frac{1}{2}$ with no isotopic or quadrupolar effects and thus provides a basically simple system for investigations of nuclear magnetism and nuclear magnetic ordering.

The lowest measured nuclear temperature was $T = 280$ pK, as deduced from the second law of thermodynamics. However by using the relation between polarization and temperature, the lowest nuclear temperature achieved can be estimated to be less than 100 pK.

The highest polarizations reached at positive temperatures were $p = 0.95 \pm 0.03$, but no indication of ordering was seen in the data. The antiferromagnetic tendency is clear, however. Compared to earlier experiments [4], the nuclear spins in rhodium were polarized to a higher degree, the relaxation rate in zero magnetic field was nearly an order of magnitude slower and the nuclear susceptibility signal was satisfactorily clean from disturbances, but yet, no anomaly attributable to nuclear magnetic ordering was observed. There remains three possibilities: a) the ground state of the nuclear-spin system of rhodium exhibits only short-range order, so that the uniform susceptibility simply resembles that of a disordered system, b) the antiferromagnetic ordering temperature really is suppressed exceptionally much below the Weiss temperature of about

1.5 nK or c) for some unknown reason the nuclear susceptibility signal did not display the characteristic anomalies like seen in some conditions in Ag [36]. The strong suppression of the Néel temperature T_N could result, in part, from fundamental geometrical frustration of an antiferromagnet in an fcc lattice, from competing dipolar and indirect exchange interactions, and from quantum fluctuations associated with the low spin 1/2.

The spin lattice relaxation time τ_1 was investigated both in intermediate and low fields. At 100 mT the data followed very well the Korringa law, giving $\kappa = 8.0 \pm 0.1$ sK. At zero field the temperature dependent component of the relaxation was about a factor of three faster, which can be accepted on a theoretical basis. Additionally the spin lattice relaxation rate had a temperature independent term, which can be attributed to the paramagnetic impurity content.

Multiple spin flips, where a single photon flips several nuclei were observed. The double-spin-flip resonance was clearly observable at both positive and negative temperatures and fitted the theoretical expectations very well. The frequency shift of the double-spin-flip peak was employed for obtaining information of the mutual interactions between the nuclear spins [9], giving a good basis for eventual theoretical studies of the spin system of rhodium. A possible trace of the triple-spin-flip peak was also observed, however, its intensity was weaker than expected from theory.

The superconducting transition of rhodium was observed, giving somewhat lower critical values of $T_c = 210$ μK and $B_c = 3.4$ μT, than reported earlier by Buchal *et al.* [5].

Measurements were made also with polarized nuclei in the superconducting state, which is usually not possible as in most superconductors $B_c > B_{\mathrm{loc}}$. In such measurements a completely new regime could be accessed, where polarized nuclei are embedded in a coherent conduction electron system. The spin lattice relaxation time was found to be always longer in the superconducting state as compared to the normal state. Additionally the superconducting state relaxation times had an unexpectedly strong polarization dependence.

5 Acknowledgements

The authors wish to thank M. Paalanen, P. Hakonen, A. Oja, and P. Hedegård for useful discussions. This work was supported by the ULTI II and ULTI III grants of the European Union and by the Academy of Finland, project numbers 42299 and 44879 (Finnish Centre of Excellence Programme, 2000-2005).

References

[1] A. S Oja and O. V. Lounasmaa. Nuclear magnetic ordering in simple metals at positive and negative temperatures. *Rev. Mod. Phys.*, 69:1–136, 1997.

[2] M. T. Huiku and M. T. Loponen. Observation of a magnetic phase transition in the nuclear spin system of metallic copper at nanokelvin temperatures. *Phys. Rev. Lett.*, 49:1288–1291, 1982.

[3] P. J. Hakonen, S. Yin, and K. K. Nummila. Phase diagram and NMR studies of antiferromagnetically ordered polycrystalline silver. *Europhys. Lett.*, 15:677–682, 1991.

[4] R. T. Vuorinen, P. J. Hakonen, W. Yao, and O. V. Lounasmaa. Susceptibility and relaxation measurements on rhodium metal at positive and negative spin temperatures in the nanokelvin range. *J. Low Temp. Phys.*, 98:449–487, 1995.

[5] Ch. Buchal, F. Pobell, R. M. Mueller, M. Kubota, and J. R. Owers-Bradley. Superconductivity of rhodium at ultralow temperatures. *Phys. Rev. Lett.*, 50:64–67, 1983.

[6] P. J. Hakonen, R. T. Vuorinen, and J. E. Martikainen. Nuclear antiferromagnetism in rhodium metal at positive and negative nanokelvin temperatures. *Phys. Rev. Lett.*, 70:2818–2821, 1993.

[7] A. S. Oja and P. Kumar. Indirect nuclear spin interactions and nuclear ordering in metals. *J. Low Temp. Phys.*, 66:155–167, 1987.

[8] A. Narath, A. T. Fromhold, Jr, and E. D. Jones. Nuclear spin relaxation in metals: rhodium, palladium, and silver. *Phys. Rev.*, 144:428–435, 1966.

[9] J. T. Tuoriniemi, T. A. Knuuttila, K. Lefmann, K. K. Nummila, W. Yao, and F.B. Rasmussen. Double-spin-flip resonance of rhodium nuclei at positive and negative spin temperatures. *Phys. Rev. Lett.*, 84:370–373, 2000.

[10] N. W. Ashcroft and N. D. Mermin. *Solid State Physics*. Holt, Rinehart and Winston, New York, 1976.

[11] W. Yao, T. A. Knuuttila, K. K. Nummila, J. E. Martikainen, A. S. Oja, and O. V. Lounasmaa. A versatile nuclear demagnetization cryostat for ultralow temperature research. *J. Low Temp. Phys.*, 120:121–150, 2000.

[12] Material-Technologie & Kristalle GmbH. Im Langenbroich 20, D-52428 Jülich.

[13] J. A. Osborn. Demagnetizing factors of the general ellipsoid. *Phys. Rev.*, 67:351–357, 1945.

[14] F. R. Fickett. Oxygen annealing of copper: A review. *Materials Science and Engineering*, 14:199–210, 1974.

[15] A. C. Ehrlich. Oxygen annealing of silver for obtaining low electrical resistivity: Technique and interpretation. *J. of Mater. Sci.*, 9:1064–1072, 1974.

[16] F. Pobell. *Matter and Methods at Low Temperatures*. Springer-Verlag, 1992.

[17] K. Lefmann, T. A. Knuuttila, J. E. Martikainen, L. T. Kuhn, and K. K. Nummila. Effect of heat treatment of pure and carbon-polluted rhodium samples on the low-temperature resistivity. *J. Mater. Sci.*, 36:839–844, 2001.

[18] Vacuumschmelze GmbH. Grüner Weg 37, 63450, Hanau, Germany.

[19] P. Jauho and P. V. Pirilä. Spin-lattice relaxation of nuclei due to conduction electrons at very low temperatures. *Phys. Rev. B*, 1:21–24, 1970.

[20] P. J. Hakonen, S. Yin, and O. V. Lounasmaa. Nuclear magnetism in silver at positive and negative absolute temperatures in the low nanokelvin range. *Phys. Rev. Lett.*, 64:2707–2710, 1990.

[21] Oxford Instruments, Ltd. Old Station Way, Eynsham OX8 1TL, UK.

[22] VTT Automation. Otakaari 7 B, P.O.Box 1304, FIN-02044 VTT, Finland.

[23] M. Goldman. *Spin Temperature and Nuclear Magnetic Resonance in Solids*. Oxford University Press, 1970.

[24] H. Ishii and P. J. Hakonen. Nuclear spin relaxation at ultralow temperatures. *Phys. Rev. B*, 59:9462–9466, 1999.

[25] A. S. Oja, A. J. Annila, and Y. Takano. Investigations of nuclear magnetism in silver down to picokelvin temperatures. I. *J. Low Temp. Phys.*, 85:1–24, 1991.

[26] A. G. Anderson. Nuclear spin absorption spectra in solids. *Phys. Rev.*, 125:1517–1527, 1962.

[27] K. I. Juntunen. Effects of eddy currents on the NMR spectra of a highly polarized metal sample. Master's thesis, Helsinki University of Technology, 2000.

[28] P. J. Hakonen and S. Yin. Investigations of nuclear magnetism in silver down to picokelvin temperatures. II. *J. Low Temp. Phys.*, 85:25–65, 1991.

[29] J. P. Ekström, J. F. Jacquinot, M. T. Loponen, J. K. Soini, and P. Kumar. Nuclear spin interaction in copper: NMR at high polarization and in low fields. *Physica*, 98B:45–52, 1979.

[30] P. L. Moyland, P. Kumar, J. Xu, and Y. Takano. Coupling of the Larmor precession to the correlated motion of pairs of nuclear spins in noble metals. *Phys. Rev. B*, 48:14020–14022, 1993.

[31] H. Cheng. Spin absorption of solids. *Phys. Rev.*, 124:1359–1367, 1961.

[32] A. G. Anderson. Nonresonant nuclear spin absorption in lithium, sodium, and aluminium. *Phys. Rev.*, 115:863–868, 1959.

[33] L. C. Hebel and C. P. Slichter. Nuclear spin relaxation in normal and superconducting aluminum. *Phys. Rev.*, 113:1504–1519, 1959.

[34] D. E. MacLaughlin. in *Solid State Physics,* edited by H. Ehrenreich, F. Seitz, and D. Turnbull, volume 31. Academic, New York, 1976.

[35] T. A. Knuuttila, J. T. Tuoriniemi, and K. Lefmann. Relaxation of polarized nuclei in superconducting rhodium. *Phys. Rev. Lett.*, 85:2573–2576, 2000.

[36] K. K. Nummila, J. T. Tuoriniemi, R. T. Vuorinen, K. Lefmann, A. Metz, and F. B. Rasmussen. Neutron diffraction studies of nuclear magnetic ordering in silver. *J. Low Temp. Phys.*, 112:73–116, 1998.